Combined 3D-QSAR and docking analysis for the design and synthesis of chalcones as potent and selective monoamine oxidase B inhibitors

Marco Mellado [a,*], César González [b], Jaime Mella [c], Luis F. Aguilar [a], Dolores Viña [d,e], Eugenio Uriarte [f,g], Mauricio Cuellar [h], Maria J. Matos [f,i,*]

[a] Facultad de Ciencias, Instituto de Química, Pontificia Universidad Católica de Valparaíso, Av. Universidad #330, Curauma, Valparaíso, Chile
[b] Departamento de Química, Universidad Técnico Federico Santa María, Av. España, 1680 Valparaíso, Chile
[c] Instituto de Química y Bioquímica, Facultad de Ciencias, Universidad de Valparaíso, Av. Gran Bretaña, 1111 Valparaíso, Chile
[d] Chronic Diseases Pharmacology Group, Center for Research in Molecular Medicine and Chronic Diseases (CIMUS), Universidade de Santiago de Compostela, 15782 Santiago de Compostela, Spain
[e] Departamento de Farmacología, Farmacia y Tecnología Farmacéutica, Universidade de Santiago de Compostela, 15782 Santiago de Compostela, Spain
[f] Departamento de Química Orgánica, Facultade de Farmacia, Universidade Santiago de Compostela, 15782 Santiago de Compostela, Spain
[g] Instituto de Ciencias Químicas Aplicadas, Universidad Autónoma de Chile, 7500912 Santiago, Chile
[h] Centro de Investigación Farmacopea Chilena, Escuela de Química y Farmacia, Facultad de Farmacia, Universidad de Valparaíso, Av. Gran Bretaña, 1093 Valparaíso, Chile
[i] CIQUP/Departamento de Química e Bioquímica, Faculdade de Ciências, Universidade do Porto, 4169-007 Porto, Portugal

ARTICLE INFO

ABSTRACT

Monoamine oxidases (MAOs) are important targets in medicinal chemistry, as their inhibition may change the levels of different neurotransmitters in the brain, and also the production of oxidative stress species. New chemical entities able to interact selectively with one of the MAO isoforms are being extensively studied, and chalcones proved to be promising molecules. In the current work, we focused our attention on the understanding of theoretical models that may predict the MAO-B activity and selectivity of new chalcones. 3D-QSAR models, in particular CoMFA and CoMSIA, and docking simulations analysis have been carried out, and their successful implementation was corroborated by studying twenty-three synthetized chalcones (151–173) based on the generated information. All the synthetized molecules proved to inhibit MAO-B, being ten out of them MAO-B potent and selective inhibitors, with IC_{50} against this isoform in the nanomolar range, being (E)-3-(4-hydroxyphenyl)-1-(2,2-dimethylchroman-6-yl)prop-2-en-1-one (152) the best MAO-B inhibitor (IC_{50} of 170 nM). Docking simulations on both MAO-A and MAO-B binding pockets, using compound 152, were carried out. Calculated affinity energy for the MAO-A was +2.3 Kcal/mol, and for the MAO-B was −10.3 Kcal/mol, justifying the MAO-B high selectivity of these compounds. Both theoretical and experimental structure–activity relationship studies were performed, and substitution patterns were established to increase MAO-B selectivity and inhibitory efficacy. Therefore, we proved that both 3D-QSAR models and molecular docking approaches enhance the probability of finding new potent and selective MAO-B inhibitors, avoiding time-consuming and costly synthesis and biological evaluations.

1. Introduction

Chalcones (Fig. 1) belong to a family of privileged structures that has been widely explored as an effective scaffold in drug discovery [1]. Pharmacophores based on this double aromatic ring system have also been widely prepared, based on the easiness and efficiency of the synthetic methodologies [2]. Both naturally occurring and synthetic chalcones have been studied for their interesting biological activities, with great potential in medicinal chemistry [3]. Antimicrobial, antitubercular, anti-inflammatory, anticancer, antioxidant, antileishmanial,

* Corresponding authors at: Facultad de Ciencias, Instituto de Química, Pontificia Universidad Católica de Valparaíso, Av. Universidad #330, Curauma, Valparaíso, Chile (M. Mellado), Departamento de Química Orgánica, Facultade de Farmacia, Universidade Santiago de Compostela, 15782 Santiago de Compostela, Spain (M.J. Matos).
E-mail addresses: marco.mellado@pucv.cl (M. Mellado), mariajoao.correiapinto@usc.es, maria.matos@fc.up.pt (M.J. Matos).
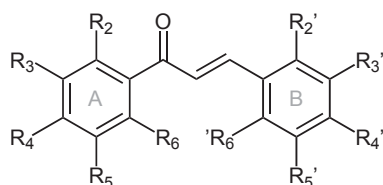
Fig. 1. Structure of the trans-chalcone, with the numbering used throughout the manuscript, and rings A and B highlighted in grey.

amongst other significant biological activities, have been attributed to chalcones derivatives and analogues [4–11].

In the last decade, huge efforts from the academic community are focused on the understanding and treatment of age-related disorders, especially neurodegenerative diseases. The development of novel and effective inhibitors of human monoamine oxidases (*h*MAOs) is still on the top of the list, due to their role in neurotransmitters' degradation and reactive oxygen species generation [12]. New chemical entities able to interact selectively with one of the MAO isoforms –MAO-A or MAO-B– binding pockets, are being extensively studied [13]. The chalcone is one of the scaffolds with great interest as *h*MAOs inhibitors [14,15]. Knowledge on the selective interaction with both isoforms has generated potent molecules in the design of new leads [16].

Based on previous results from our research group [17], in the present work, we focused our attention on the understanding of the targets, on their selectivity, and on the selection of substitution patterns that may amplify the potential of chalcones within this field. Structure-activity relationship (SAR) studies were performed based on 3D-QSAR models and docking simulations analysis of a database of one hundred and fifty molecules. Based on the theoretical approaches, the synthesis and biological evaluation of twenty-three (**151**–**173**) potent and selective MAO-B inhibitors was successfully carried out.

2. Results and discussion

For the formulation of the theoretical models, a database of one hundred and fifty chalcones was used (structures reported in Table S1). The molecules present a wide structural variability on both sides of the unsaturated system (rings A and B, Fig. 1). All the compounds span a biological activity range of more than three logarithmic units. To obtain the best CoMFA and CoMSIA models, to support the design of new molecules, a systematic sequential search was carried out (Table S2). The results of the combination of steric, electrostatic, hydrophobic, and hydrogen bond donor and acceptor fields, were evaluated. The standard criterion for the discrimination of the models was the value of q^2 higher than 0.5 [18,19]. Besides, a thorough external validation was carried out. Several parameters like r^2 of test set, and r_m^2 were calculated (Table S4). In addition, a Y-random test was performed (Table S5), obtaining better values than the established criteria.

The MAO-B inhibition values, with the predictions made by the selected CoMFA and CoMSIA models, are presented in Table S3. The experimental *versus* predictive activity graphs for the best CoMFA and CoMSIA models were created to visualize whether there is an adequate linear distribution of the predictive results for both models (Fig. 2). A good data distribution along the line $y = x$ for both CoMFA and CoMSIA in the training and test sets, was observed.

2.1. Contour map analysis

The information obtained from the SAR studies allows the design and synthesis of new promising molecules. One of the advantages of the employed 3D-QSAR technique is obtaining contour maps around the studied molecules. The analysis of the different color-polyhedra around a molecule allows understanding the main characteristics that are favorable/unfavorable for the biological activity. Since the CoMFA and
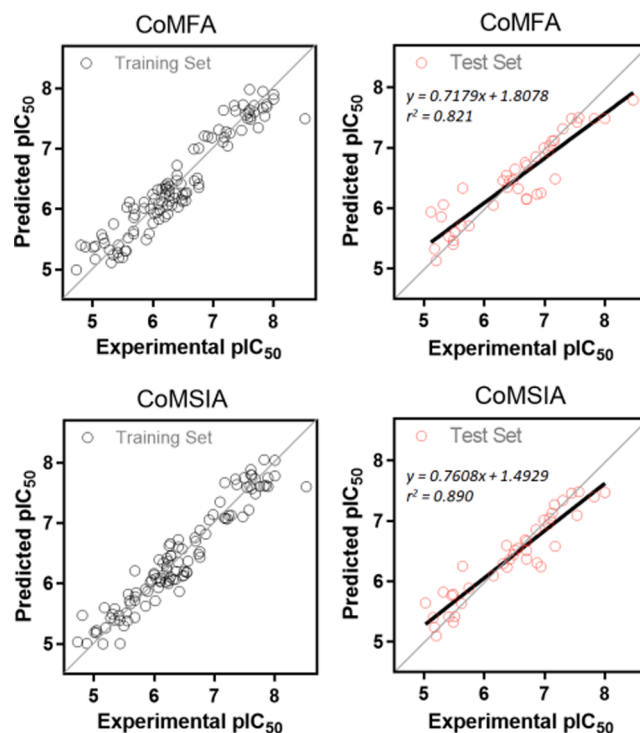

Fig. 2. Plots of experimental *versus* predicted pIC$_{50}$ values for the training (on the left, in black) and test (on the right, in red) sets. For the test set, the regression line for r^2 is shown in bold. (For interpretation of the references to color in this figure legend, the reader is referred to the web version of this article.)

CoMSIA models presented the best statistical values (Table S2), the contour maps were based on their analysis. For the visualization of the contour maps, (*E*)-1-(benzo[*d*[1,3]dioxol-5-yl)-3-(4-fluorophenyl)prop-2-en-1-one (**51**), the best MAO-B inhibitor of the training set, and (*E*)-1-(4-bromophenyl)-3-(2,3-diethoxyphenyl)prop-2-en-1-one (**139**), the less active compound of the database, were selected.

The steric contour maps analysis of CoMFA (Fig. 3A and B) and CoMSIA (Fig. 4A and B) are very similar. A green polyhedron is projected between positions 3 and 4. This means that bulky substituents at these positions of ring A favor the MAO-B inhibitory activity. As example, compounds **15**–**16**, **19**, **34**, **42**–**67**, **72**, **109**, **115**–**117**, **120**, **124**, **126**, **127**, **131**–**133**, **138**, **140** and **146** have substituents like chlorine, bromine, methoxy, ethoxy, trifluoromethyl, *N*-morpholine, benzo[*d*[1,3]dioxol-5-yl, 2,3-dihydrobenzo[*b*][1,4]dioxin-6-yl, and exhibit pIC$_{50}$ ≥ 6.5 (Table S3). Indeed, the last two types of substituents which have a fused ring such as benzo[*d*[1,3]dioxol-5-yl (compounds **42**–**54**) and 2,3-dihydrobenzo[*b*][1,4]dioxin-6-yl (compounds **55**–**67**), show potent inhibitory activity on MAO-B (pIC$_{50}$ > 7.0, Table S3). In these compounds, the bulky substituent projects into the green polyhedron (Figs. 3A and 4A). In contrast, close to position 4′ of the ring B (Figs. 3A and 4A), a yellow polyhedron is observed, indicating that a bulky substituent decreases the MAO-B inhibitory activity (i.e. compounds **5**–**9**, **13**, **22**–**23**, **36**, **38**–**41**, **101**, **103**, **105**, **110**, **111**, **113**–**114**, **119**, **121**–**123**, **137** and **141**–**150**, pIC$_{50}$ ≤ 6.5, Table S3). In this sense, compounds that present 2-furyl (i.e. **4**–**13** and **22**–**25**), 2-thiophenyl (i.e. **26**, **32** and **33**), flurbiprofen (i.e. **35**–**41**) and 1*H*-imidazol-1-yl (i.e. **98**–**105**) substituents as ring A, project at least one fragment on this yellow polyhedron, causing a decrease in the MAO-B inhibitory activity (pIC$_{50}$ ≤ 6.5, Table S3).

Positions 2′, 3′ and 4′ are oriented within the large green polyhedron (Fig. 3A, on the right), which indicates that bulky substituents at these positions favor the MAO-B inhibitory activity (i.e. compounds **10**–**12**, **24**–**26**, **32**–**34**, **43**–**72**, **115**–**117**, **124**–**127** and **130**–**136**, pIC$_{50}$ ≥ 6.5,
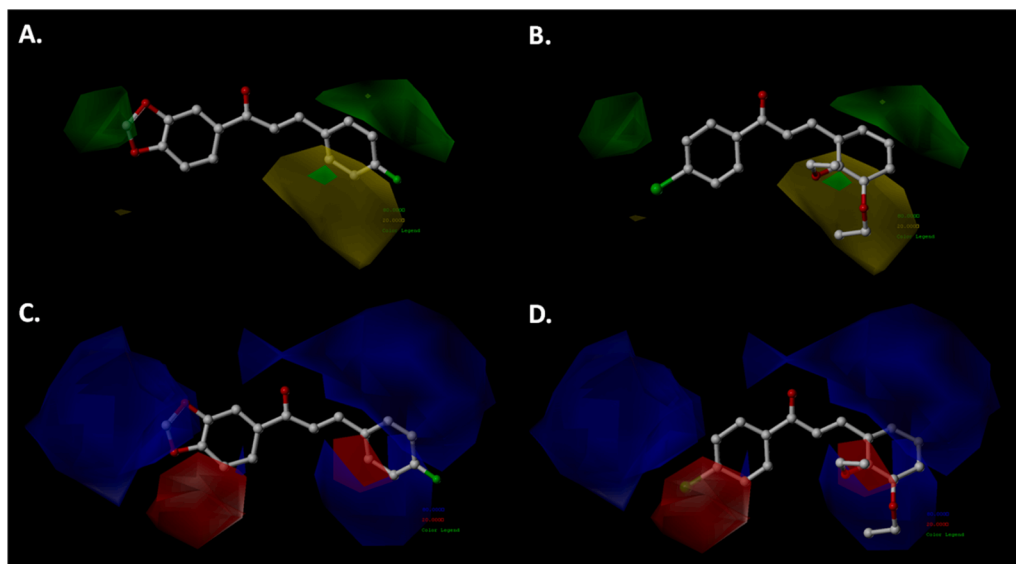
Fig. 3. CoMFA steric (**A** and **B**) and electrostatic (**C** and **D**) contour maps around the most active [(*E*)-1-(benzo[*d* [1,3]dioxol-5-yl)-3-(4-fluorophenyl) prop-2-en-1-one (**51**), on the left] and the less active [(*E*)-1-(4-bromophenyl)-3-(2,3-diethoxyphenyl)prop-2-en-1-one (**139**), on the right] compounds obtained from the training set. Color code: green, bulky groups are favorable for activity; yellow, small groups are favorable for activity; red, negative charge is favorable for activity; blue, positive charge is favorable for activity. (For interpretation of the references to color in this figure legend, the reader is referred to the web version of this article.)
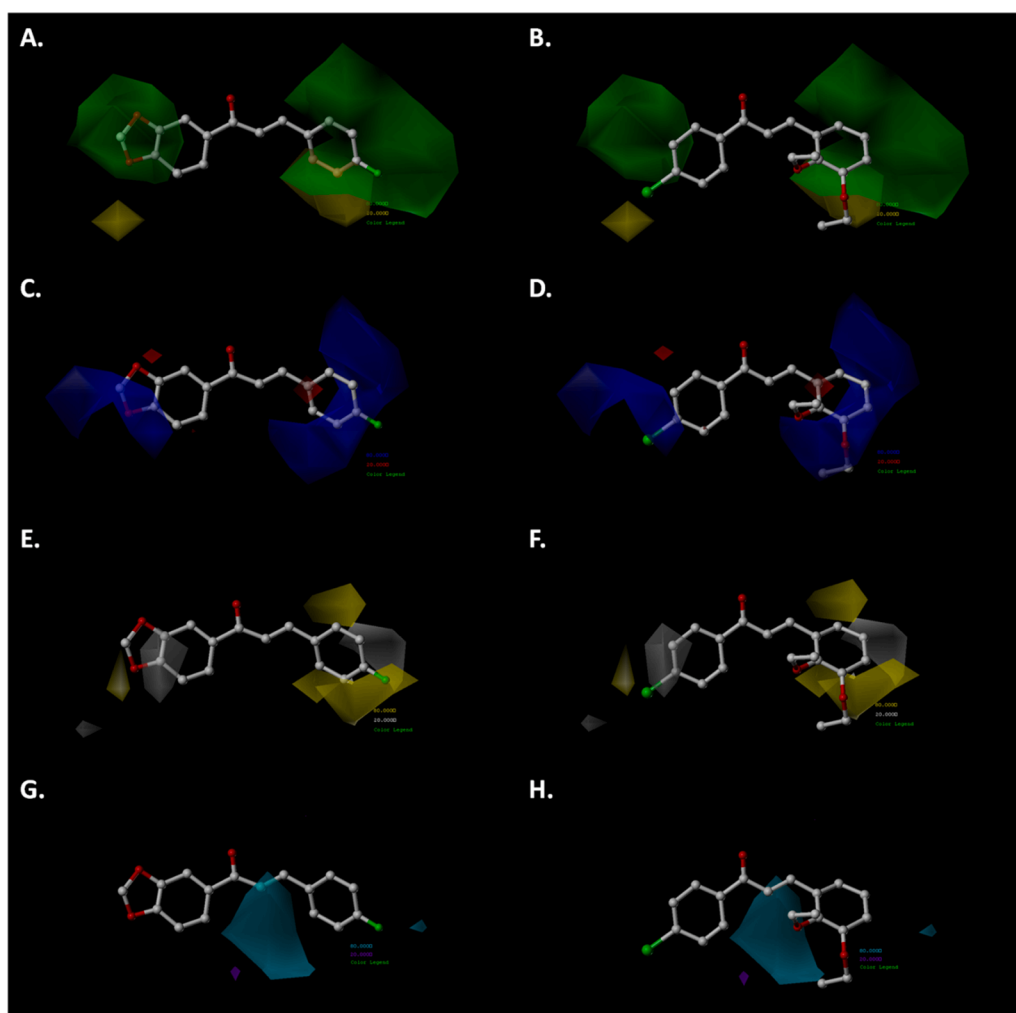
Fig. 4. CoMSIA steric (**A** and **B**), electrostatic (**C** and **D**), hydrophobic (**E** and **F**) and hydrogen bonding donor (**G** and **H**) contour maps around the most active [(*E*)-1-(benzo[*d*[1,3]dioxol-5-yl)-3-(4-fluorophenyl)prop-2-en-1-one (**51**), on the left] and the less active [(*E*)-1-(4-bromophenyl)-3-(2,3-diethoxyphenyl) prop-2-en-1-one (**139**), on the right] compounds obtained from the training set. Color code: green, bulky groups are favorable for activity; yellow, small groups are favorable for activity; red, negative charge is favorable for activity; blue, positive charge is favorable for activity. For the hydrophobic contour map: yellow, hydrophobic groups are favorable for the activity; grey, hydrophilic groups are favorable for the activity. For the hydrogen bonding donor contour map: cyan, hydrogen bonding donor groups are favorable for the activity; purple, hydrogen bonding donor groups are not favorable for the activity. (For interpretation of the references to color in this figure legend, the reader is referred to the web version of this article.)

Table S3). Additionally, positions 5′ and 6′ are projected into a yellow polyhedron, indicating that bulky substituents at these positions may decrease the MAO-B inhibitory activity (i.e. compounds **2–3**, **7–9**, **13**, **78–95**, **137** and **139**, pIC$_{50}$ ≤ 6.5, Table S3).

The electrostatic contour maps analysis of CoMFA (Fig. 3C and D) and CoMSIA (Fig. 4C and D) are very similar. A blue polyhedron extending over position 4 and its surroundings can be observed. This indicates that a deficiency of electrons favors the MAO-B inhibitory

activity of chalcones. Indeed, the introduction of heteroatoms at position 4 produces the decrease of electron density at that position. As examples, compounds with benzo[*d*[1,3]dioxol-5-yl (**42–54**) and 2,3-dihydrobenzo[*b*][1,4]dioxin-6-yl (**55–67**) as ring A, show potent MAO-B inhibitory activity (pIC$_{50}$ > 7.0, Table S3). In the case of 1*H*-imidazole-1-yl (i.e. compounds **98–105**) and carbamates (i.e. compounds **107–114**), where the electron density of the heteroatom is in resonance with the imidazole ring and with the carbamate fragment, respectively, there is a decrease in the MAO-B inhibitory activity (pIC$_{50}$ ≤ 6.5, Table S3). In this same ring, in the vicinity of the substituent linked at position 3, a red polyhedron is projected, which means that an electron-rich substituent favors the MAO-B inhibitory activity. This is consistent with the presence of oxygen atoms in benzo[*d*[1,3]dioxol-5-yl and 2,3-dihydrobenzo [*b*][1,4]dioxin-6-yl derivatives (pIC$_{50}$ > 7.0, Table S3).

A blue polyhedron extending over positions 3′ and 4′ is observed, indicating that a deficiency of electrons in these carbons increases the MAO-B inhibitory activity. Therefore, electronegative substituents attached to these carbons such as halogens, trifluoromethyl, alkyl, hydroxy, amongst others, would be favorable (i.e. compounds **10–12**, **32–33**, **43–51**, **56–57**, **62–66**, **69–70**, **72**, **117**, **120**, **124–127**, **130**, **133–136** and **146**, pIC$_{50}$ > 6.5, Table S3). Additionally, the blue polyhedron extends over the substituents at positions 2′ and 3′. Therefore, electron-deficient substituents, such as trifluoromethyl and dioxomethylene groups, where the carbon atom is projected into the blue polyhedron, favor the MAO-B inhibitory activity (compounds **11** and **124–127**, pIC$_{50}$ > 6.5, Table S3). In this same ring, a red polyhedron is projected on carbon 3 of the α,β-unsaturated carbonyl fragment, indicating that the increase in electron density on this carbon favors the MAO-B inhibitory activity, which is consistent with the structure of the heterocyclic derivatives containing the 2-furan (**14–16** and **18–20**) and 2-thiophene (**34**) moieties.

The hydrophobic contour map of the CoMSIA model is shown in Fig. 4E-F. A gray polyhedron appears in the proximity of positions 3 and 4, which means that hydrophilic substituents favor the MAO-B inhibitory activity. This is consistent with derivatives that possess pyridine and hydroxy groups (i.e. **28**, **74** and **106**, pIC$_{50}$ ~ 6.5). Furthermore, in this same ring, a yellow polyhedron extends over the vicinity of the substituent at position 4, indicating that hydrophobic substituents may favor the MAO-B inhibitory activity. This is consistent with the potent activity shown by the benzo[*d*[1,3]dioxol-5-yl (**42–54**) and the 2,3-dihydrobenzo[*b*][1,4]dioxin-6-yl derivatives (i.e. **55–67**, pIC$_{50}$ > 7.0, Table S3).

In contrast, a gray polyhedron extends in the vicinity of position 3′, which means that a hydrophobic substituent at that position does not favor the MAO-B inhibitory activity. This is consistent with the presence of chlorine, methoxy, carbamate and alkylamine substituents, as compounds **2–4**, **6**, **8**, **13**, **21–22**, **27**, **79–90**, **92–97** and **139** (pIC$_{50}$ < 6.5, Table S3). Likewise, close to the substituents at positions 2′, 4′ and 5′, a yellow polyhedron is shown, which implies that substituents with hydrophobic characteristics may favor the MAO-B inhibitory activity. Substituents such as halogens, alkyl, methoxy, dioxomethylene and bulky NR$_2$ would be favorable (i.e. compounds **10–12**, **24–26**, **32–34**, **44–47**, **49–51**, **53–54**, **57–60**, **62**, **66–70**, **100**, **115–117**, **120**, **123–127** and **146**, pIC$_{50}$ > 6.5, Table S2).

The hydrogen bond donor map obtained from the CoMSIA analysis is shown in Fig. 4G and H. A cyan polyhedron is projected under the carbonyl group of the chalcone scaffold, which means that a hydrogen bond donor promotes the MAO-B inhibitory activity. This trend is corroborated by pyrrole-chalcone derivatives (i.e. **27** and **29–31**), which have pIC$_{50}$ that vary between 5.5 and 6.1. In these cases, the hydrogen atom corresponding to the NH fragment of the pyrrole is orientated towards this polyhedron.

2.2. Molecular docking

The docking analysis was performed using the Autodock Vina

program and the crystal structure of *h*MAO-B (PDB ID: 1GOS). The results showed that (*E*)-1-(benzo[*d*[1,3]dioxol-5-yl)-3-(4-fluorophenyl) prop-2-en-1-one (**51**) has an affinity energy for this isoform of −8.8 Kcal/mol. The visualization of the result was carried out with the PyMOL and Ligplot + programs (Fig. 5).

Fig. 5 shows the general visualization of MAO-B with the best pose of compound **51** within the active site. This result is consistent with the best pose previously reported by our group [17,20]. Fig. 5B highlights the cofactor FAD600 and the Tyr435 and Tyr398 residues, both related to the inhibition of this enzyme. Indeed, the Tyr435 residue forms a hydrogen bond with the carbonyl group of the chalcone scaffold. In addition, the nitrogen atom of FAD600 shows a polar interaction with the dioxomethylene fragment of compound **51**, which stabilizes the ligands within the MAO-B active site. These interactions are key for the inhibition of this enzyme since prior oxidation of FAD600, Tyr435 and
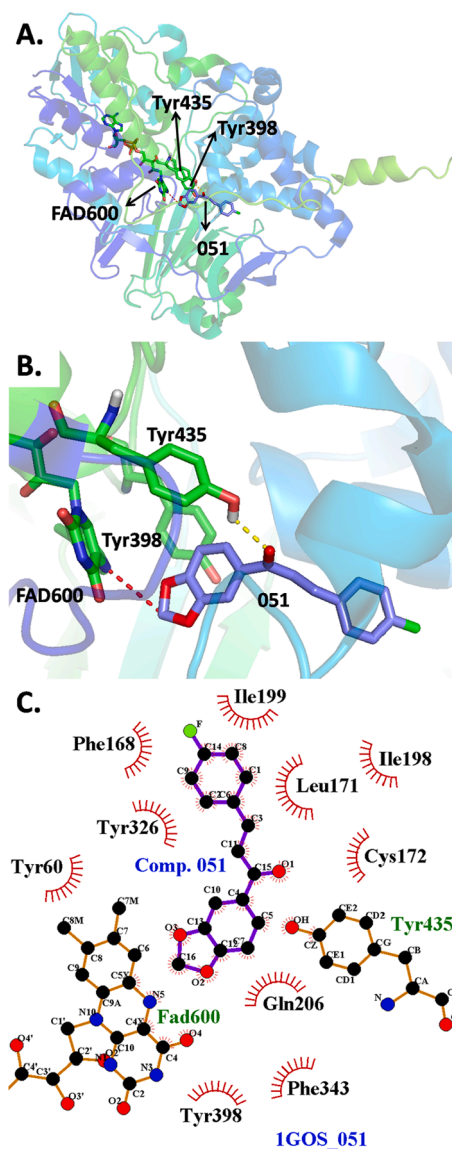

Fig. 5. Molecular docking performed with (*E*)-1-(benzo[*d*[1,3]dioxol-5-yl)-3-(4-fluorophenyl)prop-2-en-1-one (**51**). **A.** 3D overview within the active site of MAO-B. **B.** MAO-B inhibition site and key amino acid residues. **C.** Details of polar and *van der Waals* interactions established with the residues on the MAO-B active site. Hydrogen bonds are represented in yellow segmented lines. Polar interactions are. represented in red segmented lines. (For interpretation of the references to color in this figure legend, the reader is referred to the web version of this article.)

Tyr398 residues polarize the ligand [21]. Finally, as observed in Fig. 4C, ring A is oriented towards the FAD cofactor, while ring B is oriented towards Phe168 and Ile199 residues, favoring the stabilization of compound **51** within the MAO-B active site.

Comparing the molecular docking results with those obtained by 3D-QSAR, it is corroborated that a bulky element in the vicinity of positions 3 and 4 favors the MAO-B inhibition, since the Phe343 residue may improve the stabilization of the ligand within the MAO-B active site. Additionally, substituents with hydrophilic characteristics favor the MAO-B inhibition, result consistent with the potential interaction with the Tyr60 residue through polar interactions or hydrogen bonding. The results of 3D-QSAR show that an electron-rich group may establish hydrogen bonds with both Tyr60 and Gln206 residues, interactions corroborated by the docking simulations. Another important characteristic of the ring A is the presence of an electron-deficient substituent at position 4, which is consistent with the polar interaction between the cofactor FAD600 and compound **51**.

Ring B is orientated towards Leu171, Ile199, Phe168 and Cys172 residues. According to the 3D-QSAR, bulky substituents in the vicinity of positions 2′, 3′ and 4′ favor the MAO-B inhibition. This is consistent with the vicinity of Leu171, Ile199 and Phe168 residues. This could improve the stabilization of compound **51** within the MAO-B active site by *van der Waals* interactions. Near position 2′, it was determined that hydrophilic and electron-deficient substituents favor the MAO-B inhibitory activity. This is consistent with the projection of the Cys172 residue in the vicinity of this position, and the potential formation of hydrogen bonds with this residue. Another important characteristic of this ring is the closeness to Ile199 and Leu171 residues, consistent with the presence of hydrophobic substituents found in the hydrophobic contour map.

Finally, the carbonyl group is found close to the Tyr326 and Tyr398 residues. These residues could generate polar interactions and/or hydrogen bonds with the molecule. According to the 3D-QSAR, the presence of hydrogen bond donor groups under the carbonyl group favors the MAO-B inhibitory activity of compound **51**, which is consistent with the docking calculations.

2.3. Summary of the main results obtained from the theoretical models

In Fig. 6, the information on the SAR obtained from the 3D-QSAR and molecular docking models is summarized. Fulfilling the requirements of a bulky, hydrophobic group in the vicinity of positions 3 and 4 (in particular a fused ring), an electron donating atom at position 4, and hydrophobic and/or electron withdrawing/donating groups at positions 2′, 3′, 4′ and 5′, new potent MAO-B compounds may be obtained. Finally, the presence of hydrogen bonding donors at positions 2 and/or 2′ may contribute to increase the desired activity.

3. Synthesis, biological evaluation and docking calculations

To perform an experimental validation of the obtained theoretical models, the synthesis of twenty-three derivatives (Scheme 1, compounds **151**–**173**) was carried out. The compounds were synthesized based on the information obtained from the contour maps (Figs. 3 and 4), which suggested that bulky and hydrophobic groups linked to positions 3 and 4 of the chalcone scaffold, and hydrophobic and/or electron withdrawing or donating substituents at positions 2′ to 5′, would provide compounds with good activity and selectivity. Methyl, hydroxy, methoxy, fluorine, bromine and 3,4-dioxomethylene groups were selected, and strategically placed on the pharmacophoric core, based on the Craig diagram, in order to explore the chemical space as much as possible, and optimize the synthetic strategies. To obtain compounds **151**–**158**, the precursor [1-(4-hydroxy-3-(3-methylbut-2-en-1-yl)phenyl)ethan-1-one (**A**)] was previously isolated from *S. graveolens* [17,22]. Compound **A** was then stirred with formic acid to cyclize the prenyl group, obtaining compound 1-(2,2-dimethylchroman-6-yl)ethan-1-one (**B**) in very good yield (96%). This allowed obtaining a key voluminous substitution pattern that may improve the MAO-B inhibition. This compound was characterized by IR and NMR spectroscopic techniques, following previous reports from our research group [22]. To obtain compounds **159**–**165** and **166**–**173**, the commercial acetophenones, 4-methoxyacetophenone (**C**) and acetophenone (**D**) were reacted, respectively, with the appropriate benzaldehydes, in alkaline medium [23,24].

After the synthesis of the proposed compounds, their MAO-A and MAO-B inhibitory activities were evaluated by measuring the production of hydrogen peroxide (H_2O_2) from *p*-tyramine, using the Amplex® red MAO assay kit, according to previous protocols [17,25]. The experimental and predicted inhibitory MAO-B values (IC_{50} and pIC_{50}), using both CoMFA and CoMSIA models, are shown in Table 1.

All the evaluated compounds exhibited MAO-B inhibitory activity in the micro- and nanomolar ranges, being seventeen compounds selective against the MAO-B isoform. Ten compounds from this series were active against MAO-B in the nanomolar range, being the best MAO-B inhibitor the (*E*)-3-(4-hydroxyphenyl)-1-(2,2-dimethylchroman-6-yl)prop-2-en-1-one (**152**, $pIC_{50} = 6.770$), confirming the structural information obtained from both CoMFA and CoMSIA models, $pIC_{50} = 6.621$ and 6.886, respectively). In the same range of activity appear (*E*)-3-(4-methoxyphenyl)-1-(2,2-dimethylchroman-6-yl)prop-2-en-1-one (**153**), (*E*)-3-(4-hydroxy-3-methoxyphenyl)-1-(2,2-dimethylchroman-6-yl)prop-2-en-1-one (**155**), (*E*)-1-(4-methoxyphenyl)-3-(*p*-tolyl)prop-2-en-1-one (**161**), (*E*)-3-(4-hydroxyphenyl)-1-(4-methoxyphenyl)prop-2-en-1-one (**162**), (*E*)-1-phenyl-3-(*p*-tolyl)prop-2-en-1-one (**168**), (*E*)-3-(4-hydroxyphenyl)-1-phenylprop-2-en-1-one (**169**) and (*E*)-3-(4-methoxyphenyl)-1-phenylprop-2-en-1-one (**170**), proving that the presence of electron donating groups at position 4′ of the chalcone scaffold is indeed interesting for the studied activity. The only exception within the series are (*E*)-1-(4-methoxyphenyl)-3-phenylprop-2-en-1-one (**159**), without substitutions in the ring B, and (*E*)-3-(5-bromo-2-fluorophenyl)-1-(2,2-dimethylchroman-6-yl)prop-2-en-1-one (**154**), presenting two halogens at positions 2′ and 5′. Despite being important structural differences, these results are also aligned with the theoretical prediction.

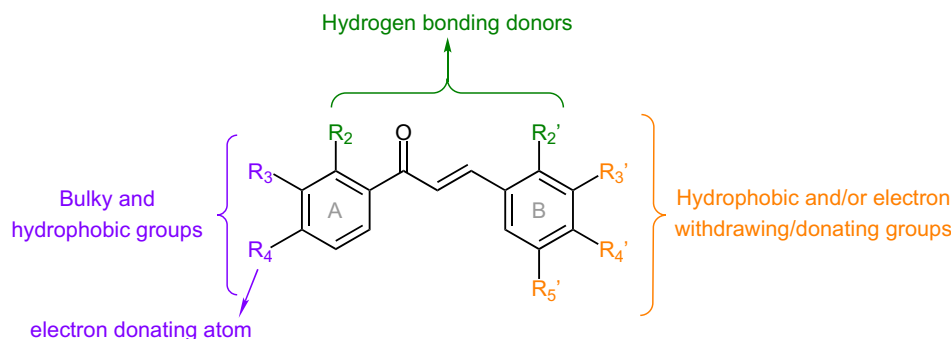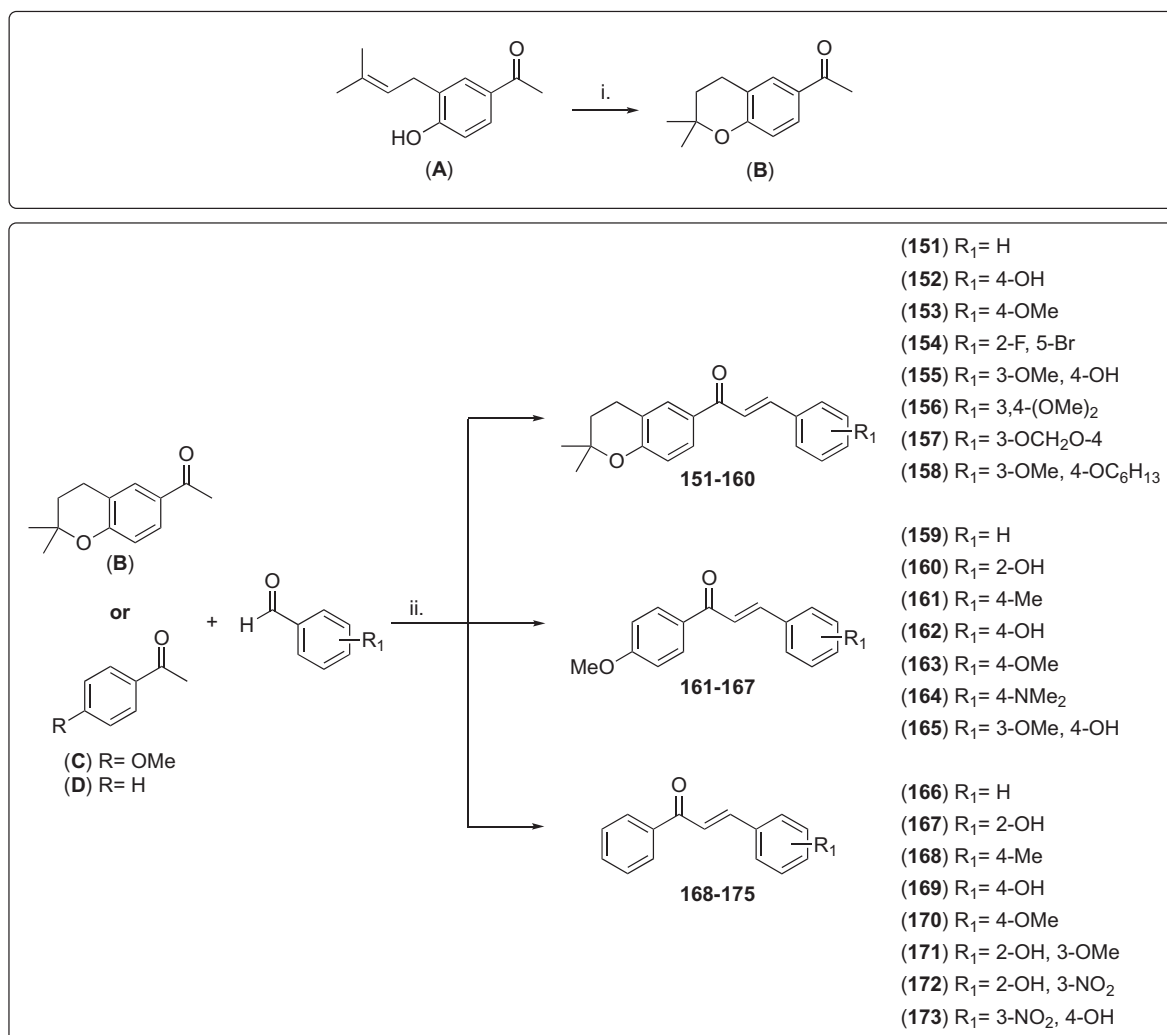In the specific case of compounds **152**, **153** and **154**, the three have a

Fig. 6. Summary of the main theoretical structure–activity relationships for the MAO-B inhibition found in the present study.

Scheme 1. Synthetic route to obtain compounds **151**–**173**. Reagents and conditions: (i) HCO$_2$H, overnight, rt. (ii) NaOH/EtOH (20% m/v), 48 h, rt.

hydrophobic and bulky group at both positions 3 and 4, having an electronegative substituent attached directly to the carbon 4. Compounds **159**, **161** and **162** present only an electron donating group at position 4, being the substituent a methoxy group. Compounds **161** and **162** present additionally a hydrophobic and electron donating group at position 4′ of the chalcone scaffold. These are two of the most active compounds within the series, proving that the combination of substituents in *para* position at both rings may be ideal to increase the MAO-B inhibitory activity. Comparing compounds **152** and **162**, the only structural difference is the presence of a pyran ring attached to the ring A. This voluminous substituent makes compound **152** exhibit a two-fold higher MAO-B inhibitory activity comparing to compound **162**. Even if the pyran ring seems to play an important role for the activity, these are the two best compounds of the studied series. Finally, compounds **168**, **169** and **170** do not present any substituent in the ring A, proving that substituents in the ring B, specially at *para* position, may play themselves an important role for the activity.

As said before, the evaluated compounds showed experimental selectivity towards *h*MAO-B. The high selectivity against this isoform is a subject of high interest for the future design of MAO-B inhibitors. Therefore, a molecular docking analysis was performed simulating the interaction of compound **152** with the active site of both MAO isoforms. According to Abad and co-workers, the ligand was positioned between Tyr435 and Tyr398 residues, and perpendicular to the FAD cofactor in the MAO-B binding pocket (Fig. 7D and 7E) [21]. Then, applying the same criteria for the MAO-A isoform, the ligand was located between

Tyr407 and Tyr444 residues, perpendicular to the FAD (Fig. 7A and 7B). Calculated affinity energy for the MAO-A isoform was + 2.3 Kcal/mol. This is consistent with a non-spontaneous process and non-inhibition of this isoform. This result may be due to repulsions of the dihydrochroman fragment with the Tyr407, Tyr444 and Asn181 residues (Fig. S3). In the MAO-B study, the calculated affinity energy for compound **152** was −10.3 Kcal/mol. This is consistent with a spontaneous process and the potent MAO-B inhibitory activity of this compound.

Fig. 8 presents the graph of the experimental *versus* predicted activity for the synthesized compounds **151**–**173**. All the compounds are within one logarithmic unit of residual value. The best predictions are for the most active compounds, with pIC$_{50}$ > 6.0. For compounds presenting pIC$_{50}$ < 6.0, both models tended to overestimate the predicted activity values.

Finally, analyzing the experimental data obtained, the presence of electron donating and bulky substituents at positions 3 and 4 of the chalcone scaffold seems to be important for the studied activity. In addition, the presence of an electron donating group at position 4′, in this case non-bulky groups, may be very important to enhance the inhibitory activity. Finally, the presence of a hydrogen bond donor at position 2′ and a halogen at positions 2′ and/or 5′ may contribute to increase the desired activity. A summary of the best substitution patterns is shown in Fig. 9.

Table 1

Experimental MAO-A and MAO-B inhibition values (IC_{50} and pIC_{50}) and predicted activity on MAO-B (pIC_{50} CoMFA and pIC_{50} CoMSIA) for compounds **151–173**.

Compounds	IC_{50} (μM)		MAO-B pIC_{50}		
	MAO-A	MAO-B	Experimental	CoMFA	CoMSIA
151	>100	2.0 ± 0.10	5.699	5.669	5.653
152	>100	0.17 ± 0.01	6.770	6.621	6.886
153	>100	0.93 ± 0.07	6.032	5.908	6.029
154	>100	0.39 ± 0.02	6.409	6.405	6.494
155	8.20 ± 1.53	0.70 ± 0.08	6.155	6.188	6.121
156	11.92 ± 2.69	1.79 ± 0.03	5.747	5.680	5.823
157	49.80 ± 5.87	1.46 ± 0.08	5.836	5.905	6.116
158	11.92 ± 2.69	1.79 ± 0.04	5.747	5.900	5.664
159	>100	0.43 ± 0.04	6.367	6.328	6.391
160	>100	6.34 ± 0.33	5.198	5.907	6.048
161	>100	0.21 ± 0.03	6.678	6.613	6.621
162	>100	0.35 ± 0.03	6.456	6.528	6.459
163	>100	3.41 ± 0.12	5.467	5.988	5.975
164	>100	2.29 ± 0.21	5.640	6.129	6.240
165	4.18 ± 1.49	2.22 ± 0.08	5.654	6.499	6.320
166	>100	3.27 ± 0.15	5.485	6.141	6.361
167	>100	4.0 ± 0.39	5.398	5.980	6.163
168	>100	0.43 ± 0.06	6.367	6.206	6.412
169	>100	0.44 ± 0.02	6.357	6.405	6.290
170	>100	0.99 ± 0.12	6.004	6.058	6.129
171	6.92 ± 0.73	2.53 ± 0.27	5.597	5.860	6.060
172	>100	2.92 ± 0.20	5.535	5.869	6.413
173	>100	5.58 ± 0.42	5.253	6.277	5.904
Selegiline	67.25 ± 1.02	0.020 ± 0.009	7.699		
Iproniazide	6.56 ± 0.76	7.54 ± 0.36	5.123		

4. Conclusions

In the current study, robust 3D-QSAR models –CoMFA and CoMSIA– were constructed based on a database of one hundred and fifty compounds previously reported in scientific articles. All the molecules present a chalcone scaffold, known for their MAO inhibitory activity. The best models obtained were, afterwards, internal and externally validated. The best CoMFA model presented a combination of both steric and electrostatic fields, with a q^2 value of 0.851, and the best CoMSIA model presented a q^2 value of 0.813. The reliability of the models was tested, and both present good external predictive capabilities. To experimentally validate the models, twenty-three new derivatives (compounds **151–173**) have been designed, synthesized and evaluated. Ten new derivates proved to be potent and selective MAO-B inhibitors, presenting activities in the nanomolar range. The most powerful and selective compound within this series was (*E*)-3-(4-hydroxyphenyl)-1-(2,2-dimethylchroman-6-yl)prop-2-en-1-one (**152**), presenting a MAO-B IC_{50} of 170 nM. Docking simulations have also been taken into account

in the current study, and a MAO-A *versus* MAO-B comparative study, using compound **152**, was performed. Calculated affinity energy for the MAO-A isoform was + 2.3 Kcal/mol, and for the MAO-B was −10.3 Kcal/mol. Together with the residues' interactions nature, these may explain the high MAO-B selectivity of this family of compounds. Some important structural features that may be conditioning the biological activity can be highlighted analyzing all the theoretical data together. Hydrophobic groups, like ethers, may be present at both 3 and 4 positions of the chalcone scaffold. In addition, hydrophobic and electron donating substituents, like halogens, hydroxyl, methyl or methoxy groups, at positions 2′, 4′ or 5′, may be important in the design of new lead compounds. Based on all these data, it can be concluded that 3D-QSAR models, together with docking simulations, constitute robust tools for the design of new MAO-B inhibitors based on the chalcone scaffold.

5. Experimental section

5.1. Theoretical calculations

The 3D-QSAR study (CoMFA and CoMSIA models) was carried out using a dataset of 150 compounds, according to the previously reported procedure [26,27]. The molecular docking analysis was carried out using the compounds **51** and **152** and MAO crystal structure (PDB code 2Z5Y for MAO-A and PDB code 1GOS for MAO-B) [28,29], with the AutoDock vina program [30], and the results were processed using Pymol [31] and LigPlot + software [32,33]. All details for 3D-QSAR study, as well as the molecular docking, are included in the supplementary material.

6. General information

All reagents were purchased from Sigma-Aldrich or Merck and used without further purification. All solvents were commercially available grade. Reaction mixtures were purified by flash column chromatography using silica gel high purity grade (Merck grade 9385 pore size 60 Å, 230–400 mesh particle size). Reaction mixtures were analyzed by analytical thin-layer chromatography (TLC) using plates precoated with silica gel (Merck 60 F254, 0.25 mm). Visualization was accomplished with UV light (254 nm) or sulfuric acid (H_2SO_4:MeOH, 5:95). The recorded range of the IR spectra was 600–4000 cm^{-1}, and all samples were examined using the ATR (attenuated total reflectance) system. ^1H NMR (400.13 MHz), ^{13}C NMR (100.6 MHz), spectra were recorded on a Bruker Avance 400 Digital NMR spectrometer (Berlin, Germany) using the stated solvents ($CDCl_3$ or Acetone-d_6), using tetramethylsilane (TMS) as an internal standard. Chemical shifts were reported in parts per million (ppm) on the δ scale from an internal standard (NMR descriptions: s, singlet; bs, broad singlet; d, doublet; dd, double doublet; t, triplet; m, multiplet). Mass spectroscopy was performed using a Hewlett-Packard 5988A spectrometer. This system is an automated service utilizing electron impact (EI) ionization.

6.1. Chemistry

Plant material and extraction procedure. *Senecio graveolens* was collected from an area near Chungara Lake at 4500 m.a.s.l. (Chile). The dry plant material (180 g) was macerated in 95% ethanol (2 × 500 mL) for 72 h, according to the procedures described in our previous reports [17,22].

6.2. Synthetic procedures

(4-Hydroxy-3-(3-methylbut-2-enyl)phenyl)ethenone(A). This compound was separated from the dry methanol extract (52.8 g) by column chromatography using hexane/EtOAc (9:1), obtaining a pale yellow solid (1.09 g). Mp 95–96 °C. The spectroscopic information (IR,
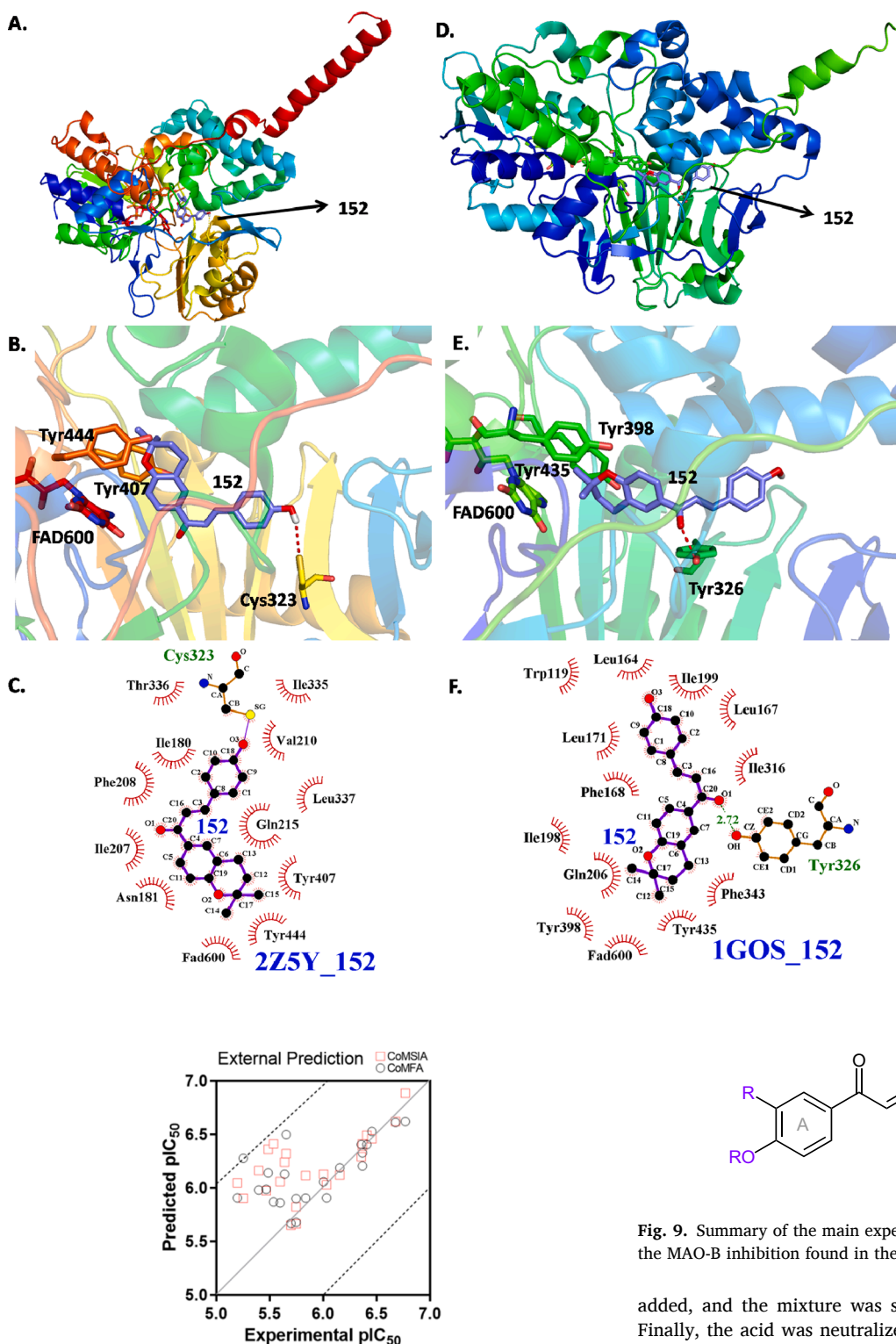
Fig. 7. Molecular docking of (*E*)-3-(4-hydroxyphenyl)-1-(2,2-dimethylchroman-6-yl)prop-2-en-1-one (**152**) on MAO-A and MAO-B. **A.** 3D overview inside the active site of MAO-A. **B.** MAO-A inhibition site and key amino acid residues. **C.** Details of polar and *van der Waals* interactions established with the MAO-A active site. **D.** 3D overview inside the active site of MAO-B. **E.** MAO-B inhibition site and key amino acid residues. **F.** Details of polar and *van der Waals* interactions established with the MAO-B active site.

Fig. 8. Values of experimental *versus* predicted MAO-B inhibitory activity for the synthesized compounds (**151–173**). Color code: black spheres, CoMFA predictions; red squares, CoMSIA predictions. (For interpretation of the references to color in this figure legend, the reader is referred to the web version of this article.)

Fig. 9. Summary of the main experimental structure–activity relationships for the MAO-B inhibition found in the present study.

^{1}H NMR and ^{13}C NMR) analysis results were consistent with previous reports [17,22].

1-(2,2-Dimethylchroman-6-yl)ethanone(B). In a 100 mL round-bottomed flask, compound **A** (0.5 g) and formic acid (15 mL) were added, and the mixture was stirred overnight at room temperature. Finally, the acid was neutralized using Na_2CO_3 5%. This mixture was extracted with EtOAc (3x50 mL), and the organic layer was dried with Na_2SO_4 and separated by column chromatography using hexane/EtOAc (8:2) obtaining a colorless solid (0.48 g). Yield: 96%. Mp 91–92 °C. The spectroscopic information (IR, ^{1}H NMR and ^{13}C NMR) analysis results were consistent with the previous report [22].

General procedure for chalcone synthesis (151–173). To a dry 100 mL round-bottomed flask, semisynthetic acetophenone **B** or commercial acetophenone **C** or **D** (250 mg, between 1.22 and 2.08 mmol) and corresponding benzaldehyde (1.2 equiv.) were added, and then solubilized in ethanol (5 mL). A NaOH 20% m/v solution (in 10 mL of ethanol) was added, and the mixture was stirred for 48 h. To stop the

reaction, 5% HCl solution was added until pH ~ 7, and the mixture was extracted with EtOAc (3x30 mL). The organic layer was dried with Na$_2$SO$_4$, filtered, and separated by column chromatography using a hexane/EtOAc, obtaining compounds **151**–**173** in yields between 27 and 99%.

(E)-1-(2,2-Dimethylchroman-6-yl)-3-phenylprop-2-en-1-one (151). Yield: 87%. Mp 85–87 °C. IR: 3050, 2975, 2938, 1659, 1604, 1574, 1495, 1448, 1336, 1258, 1230 cm^{-1}. ^{1}H NMR (CDCl$_3$): 7.83 (1H, s), 7.82 (1H, d, *J* = 2.6 Hz), 7.80 (1H, d, *J* = 15.7 Hz, Hβ), 7.65–7.62 (1H, m), 7.56 (1H, d, *J* = 15.7 Hz, Hα), 7.41–7.39 (4H, m), 6.86 (1H, d, *J* = 8.2 Hz), 2.85 (2H, t, *J* = 6.7 Hz, CH$_2$), 1.85 (2H, t, *J* = 6.7 Hz, CH$_2$), 1.37 (6H, s, 2xCH$_3$). ^{13}C NMR (CDCl$_3$): 188.7, 158.5, 143.4, 135.1, 130.8, 130.1, 128.9, 128.8, 128.4, 128.3, 121.9, 120.9, 117.3, 75.5, 32.5, 26.9, 22.3. EI-MS *m/z* (%): 292 (M$^+$, 100) [22].

(E)-3-(4-Hydroxyphenyl)-1-(2,2-dimethylchroman-6-yl)prop-2-en-1-one (152). Yield: 27%. Mp 158–160 °C. IR: 3226, 2971, 2941, 1647, 1602, 1574, 1512, 1446, 1343, 1321, 1231 cm^{-1}. ^{1}H NMR (CDCl$_3$): 7.83 (1H, s), 7.81 (4H, s), 7.76 (1H, d, *J* = 15.5 Hz, Hβ), 7.52 (2H, d, *J* = 8.4 Hz), 7.42 (1H, d, *J* = 15.5 Hz, Hα), 6.92 (2H, d, *J* = 8.4 Hz), 6.85 (1H, d, *J* = 8.5 Hz), 2.84 (2H, t, *J* = 6.7 Hz, CH$_2$), 1.84 (2H, t, *J* = 6.7 Hz, CH$_2$), 1.36 (6H, s, 2xCH$_3$). ^{13}C NMR (CDCl$_3$): 190.0, 158.7, 144.5, 132.5, 131.0, 130.4, 128.6, 127.3, 121.0, 119.2, 117.4, 116.1, 75.7, 32.5, 26.9, 22.4. EI-MS *m/z* (%): 308 (M$^+$, 100) [22,34].

(E)-3-(4-Methoxyphenyl)-1-(2,2-dimethylchroman-6-yl)prop-2-en-1-one (153). Yield: 96%. Mp 79–81 °C. IR: 3082, 2975, 1655, 1589, 1510, 1492, 1338, 1318, 1227 cm^{-1}. ^{1}H NMR (CDCl$_3$): 7.83 (1H, s), 7.81 (1H, s), 7.77 (1H, d, *J* = 15.6 Hz, Hβ), 7.60 (2H, d, *J* = 8.7 Hz), 7.43 (1H, d, *J* = 15.6 Hz, Hα), 6.93 (2H, d, *J* = 8.7 Hz), 6.84 (1H, d, *J* = 8.4 Hz), 3.85 (3H, s, OCH$_3$), 2.85 (2H, t, *J* = 6.7 Hz, CH$_2$), 1.85 (2H, t, *J* = 6.7 Hz, CH$_2$), 1.37 (6H, s, 2xCH$_3$). ^{13}C NMR (CDCl$_3$): 188.9, 161.4, 158.4, 143.4, 130.7, 130.4, 130.0, 128.3, 127.9, 120.9, 119.7, 117.2, 114.3, 77.5, 55.4, 32.5, 26.9, 22.3. EI-MS *m/z* (%): 322 (M$^+$, 100) [22].

(E)-3-(5-Bromo-2-fluorophenyl)-1-(2,2-dimethylchroman-6-yl) prop-2-en-1-one (154). Yield: 98%. Mp 124–125 °C. IR: 3053, 2978, 2944, 1657, 1609, 1544, 1484, 1453, 1311, 1234 cm^{-1}. ^{1}H NMR (CDCl$_3$): 7.89 (1H, d, *J* = 2.2 Hz), 7.81 (1H, s), 7.76 (1H, d, *J* = 15.9 Hz, Hβ), 7.73 (1H, d, *J* = 2.4 Hz), 7.60 (1H, d, *J* = 15.9 Hz, Hα), 7.37–7.41 (1H, m), 6.97 (1H, t, *J* = 9.4 Hz), 6.82 (1H, d, *J* = 8.2 Hz), 2.82 (2H, t, *J* = 6.7 Hz, CH$_2$), 1.82 (2H, t, *J* = 6.7 Hz, CH$_2$), 1.34 (6H, s, 2xCH$_3$). ^{13}C NMR (CDCl$_3$): 187.8, 161.6, 158.7, 134.1, 133.8, 133.7, 131.5, 130.8, 129.5, 128.4, 125.2, 120.9, 117.8, 117.3, 116.8, 75.5, 32.3, 26.7, 22.2. EI-MS *m/z* (%): 388 (M$^+$, 8), 199 (100). HR-EI-MS: 388.0474 calc, found 388.0417 (Δ = 0.0057).

(E)-3-(4-Hydroxy-3-methoxyphenyl)-1-(2,2-dimethylchroman-6-yl)prop-2-en-1-one (155). Yield: 72%. Mp 77–79 °C. IR: 3300, 2935, 1654, 1576, 1509, 1455, 1371, 1315, 1251 cm^{-1}. ^{1}H NMR (CDCl$_3$): 7.83 (1H, s), 7.80 (1H, s), 7.73 (1H, d, *J* = 15.6 Hz, Hβ), 7.39 (1H, d, *J* = 15.6 Hz, Hα), 7.21 (1H, d, *J* = 8.3 Hz), 7.12 (1H, s), 6.94 (1H, d, *J* = 8.2 Hz), 6.84 (1H, d, *J* = 8.3 Hz), 6.03 (1H, bs, OH), 3.95 (3H, s, OCH$_3$), 2.85 (2H, t, *J* = 6.7 Hz, CH$_2$), 1.85 (2H, t, *J* = 6.7 Hz, CH$_2$), 1.36 (6H, s, 2xCH$_3$). ^{13}C NMR (CDCl$_3$): 188.9, 158.4, 148.0, 146.8, 144.0, 130.7, 130.3, 128.3, 127.7, 123.0, 121.0, 119.7, 117.2, 114.8, 110.1, 75.5, 56.0, 32.5, 26.9, 22.4. EI-MS *m/z* (%): 388 (M$^+$, 100). HR-EI-MS: 338.1518 calc, found 388.1426 (Δ = 0.0092).

(E)-3-(3,4-Dimethoxyphenyl)-1-(2,2-dimethylchroman-6-yl) prop-2-en-1-one (156). Yield: 42%. Mp 82–85 °C. IR: 3073, 2970, 2937, 1654, 1580, 1514, 1500, 1442, 1316, 1248, 1225 cm^{-1}. ^{1}H NMR (CDCl$_3$): 7.83 (1H, s), 7.80 (1H, s), 7.74 (1H, d, *J* = 15.6 Hz, Hβ), 7.40 (1H, d, *J* = 15.6 Hz, Hα), 7.22 (1H, dd, *J* = 8.3, 1.8 Hz), 7.15 (1H, d, *J* = 1.8 Hz), 6.89 (1H, d, *J* = 8.3 Hz), 6.84 (1H, d, *J* = 8.3 Hz), 3.95 (3H, s, OCH$_3$), 3.92 (3H, s, OCH$_3$), 2.85 (2H, t, *J* = 6.7 Hz, CH$_2$), 1.85 (2H, t, *J* = 6.7 Hz, CH$_2$), 1,63 (6H, s, 2xCH$_3$). ^{13}C NMR (CDCl$_3$): 188.8, 158.4, 151.1, 149.1, 143.7, 130.7, 130.3, 128.3, 128.1, 122.8, 120.9, 119.9, 117.2, 111.1, 110.1, 75.5, 55.9, 32.5, 26.9, 26.8, 22.3. EI-MS *m/z* (%): 352 (M$^+$, 100). HR-EI-MS: 352.1675 calc, found 352.1670 (Δ = 0.0005).

(E)-3-(Benzo [*d* [1,3] dioxol-5-yl)-1-(2,2-dimethylchroman-6-yl)

prop-2-en-1-one (157). Yield: 72%. Mp 158–159 °C. IR: 3052, 2967, 2941, 1652, 1604, 1576, 1490, 1446, 1360, 1320, 1233 cm^{-1}. ^{1}H NMR (CDCl$_3$): 7.82 (1H, s), 7.80 (1H, s), 7.72 (1H, d, *J* = 15.6 Hz, Hβ), 7.39 (1H, d, *J* = 15.6 Hz, Hα), 7.17 (1H, s), 7.12 (1H, d, *J* = 8.0 Hz), 6.84 (1H, d, *J* = 8.2 Hz), 6.83 (1H, d, *J* = 8.0 Hz), 6.02 (2H, s, OCH$_2$O), 2.85 (2H, t, *J* = 6.7 Hz, CH$_2$), 1.85 (2H, t, *J* = 6.7 Hz, CH$_2$), 1.37 (6H, s, 2xCH$_3$). ^{13}C NMR (CDCl$_3$): 188.7, 158.5, 149.6, 148.3, 143.4, 130.7, 130.2, 129.6, 128.3, 124.9, 120.9, 120.0, 117.3, 108.6, 106.2, 101.5, 75.5, 32.5, 26.9, 22.4. EI-MS *m/z* (%): 336 (M$^+$, 100) [22].

(E)-3-(4-Hexyloxy-3-methoxyphenyl)-1-(2,2-dimethylchroman-6-yl)prop-2-en-1-one (158). Yield: 59%. IR: 3068, 2935, 1654, 1576, 1509, 1424, 1251, 1234 cm^{-1}. ^{1}H NMR (CDCl$_3$): 7.83 (1H, s), 7.80 (1H, s), 7.73 (1H, d, *J* = 15.5 Hz, Hβ), 7.40 (1H, d, *J* = 15.5 Hz, Hα), 7.19 (1H, dd, *J* = 8.3, 1.6 Hz), 7.15 (1H, d, *J* = 1.6 Hz), 6.87 (1H, d, *J* = 8.3 Hz), 6.83 (1H, d, *J* = 8.3 Hz), 4.04 (2H, t, *J* = 6.8 Hz, CH$_2$), 3.92 (3H, s, OCH$_3$), 2.84 (2H, t, *J* = 6.7 Hz, CH$_2$), 1.83 (2H, t, *J* = 6.7 Hz, CH$_2$), 1.85 (2H, t, *J* = 6.8 Hz, CH$_2$), 1.45 (2H, t, *J* = 6.8 Hz, CH$_2$), 1.35 (6H, s, 2xCH$_3$), 1.36–1.32 (4H, m, 2xCH$_2$), 0.88 (3H, t, *J* = 6.8 Hz, CH$_3$). ^{13}C NMR (CDCl$_3$): 188.8, 158.3, 150.8, 149.4, 143.8, 130.7, 130.3, 128.2, 127.9, 122.8, 120.9, 119.7, 117.1, 112.4, 110.7, 75.4, 68.9, 56.0, 32.5, 31.5, 28.9, 26.8, 25.5, 22.5, 13.9. EI-MS *m/z* (%): 422 (M$^+$, 100). HR-EI-MS: 422.2457 calc, found 422.2370 (Δ = 0.0087).

(E)-1-(4-Methoxyphenyl)-3-phenylprop-2-en-1-one (159). Yield: 68%. Mp 92–96 °C. IR: 3078, 2972, 2954, 1655, 1603, 1558, 1508, 1448, 1241, 1190 cm^{-1}. ^{1}H NMR (CDCl$_3$): 8.05 (2H, d, *J* = 8.7 Hz), 7.81 (1H, d, *J* = 15.6 Hz, Hβ), 7.64 (2H, m), 7.55 (1H, d, *J* = 15.6 Hz, Hα), 7.38–7.43 (3H, m), 6.98 (2H, d, *J* = 8.7 Hz), 3.88 (3H, s, OCH$_3$). ^{13}C NMR (CDCl$_3$): 188.6, 163.4, 143.9, 135.0, 131.0, 130.8, 130.3, 128.9, 128.3, 121.8, 113.8, 55.4. EI-MS *m/z* (%): 238 (M$^+$, 100) [23].

(E)-3-(2-Hydroxyphenyl)-1-(4-methoxyphenyl)prop-2-en-1-one (160). Yield: 44%. Mp 149–151 °C. IR: 3284, 3074, 2922, 1602, 1555, 1506, 1362, 1230, 1202 cm^{-1}. ^{1}H NMR (CDCl$_3$): 8.17 (1H, d, *J* = 15.9 Hz, Hβ), 8.06 (2H, d, *J* = 8.8 Hz), 7.70 (1H, d, *J* = 15.9 Hz, Hα), 7.60 (1H, d, *J* = 8.0 Hz), 7.27 (1H, t, *J* = 8.0 Hz), 6.99 (2H, d, *J* = 8.8 Hz), 6.96 (1H, t, *J* = 8.0 Hz), 6.92 (1H, d, *J* = 8.0 Hz), 6.55 (1H, bs, OH), 3.90 (3H, s, OCH$_3$). ^{13}C NMR (CDCl$_3$): 190.1, 163.5, 155.8, 140.1, 131.6, 131.2, 131.0, 129.2, 122.5, 122.4, 120.8, 116.7, 113.8, 55.5. EI-MS *m/z* (%): 254 (M$^+$, 100) [23].

(E)-1-(4-Methoxyphenyl)-3-(*p*-tolyl)prop-2-en-1-one (161). Yield: 99%. Mp 120–124 °C. IR: 3078, 2975, 2936, 1654, 1596, 1562, 1508, 1417, 1246, 1224, 1170 cm^{-1}. ^{1}H NMR (CDCl$_3$): 8.04 (2H, d, *J* = 8.8 Hz), 7.79 (1H, d, *J* = 15.6 Hz, Hβ), 7.55 (2H, d, *J* = 8.1 Hz), 7.51 (1H, d, *J* = 15.6 Hz, Hα), 7.22 (2H, d, *J* = 8.1 Hz), 6.98 (2H, d, *J* = 8.8 Hz), 3.89 (3H, s, OCH$_3$), 2.39 (3H, s, CH$_3$). ^{13}C NMR (CDCl$_3$): 188.8, 163.3, 144.0, 140.8, 132.3, 131.2, 130.7, 129.6, 128.4, 120.8, 113.8, 55.5, 21.5. EI-MS *m/z* (%): 252 (M$^+$, 100) [23].

(E)-3-(4-Hydroxyphenyl)-1-(4-methoxyphenyl)prop-2-en-1-one (162). Yield: 62%. Mp 184–186 °C. IR: 3266, 3086, 2949, 1668, 1605, 1558, 1531, 1229, 1146 cm^{-1}. ^{1}H NMR (CDCl$_3$): 8.03 (2H, d, *J* = 8.9 Hz), 7.77 (1H, d, *J* = 15.6 Hz, Hβ), 7.56 (2H, d, *J* = 8.4 Hz), 7.42 (1H, d, *J* = 15.6 Hz, Hα), 6.98 (2H, d, *J* = 8.9 Hz), 6.88 (2H, d, *J* = 8.4 Hz), 3.89 (3H, s, OCH$_3$). ^{13}C NMR (CDCl$_3$): 188.9, 163.3, 157.7, 143.8, 131.3, 130.7, 130.3, 128.0, 119.7, 115.9, 113.8, 55.5. EI-MS *m/z* (%): 254 (M$^+$, 85), 135 (1 0 0) [23].

(E)-1,3-Bis(4-methoxyphenyl)prop-2-en-1-one (163). Yield: 99%. Mp 97–101 °C. IR: 3062, 2945, 2931, 1654, 1590, 1569, 1509, 1457, 1420, 1246, 1212 cm^{-1}. ^{1}H NMR (CDCl$_3$): 8.03 (2H, d, *J* = 8.8 Hz), 7.77 (1H, d, *J* = 15.6 Hz, Hβ), 7.59 (2H, d, *J* = 8.7 Hz), 7.42 (1H, d, *J* = 15.6 Hz, Hα), 6.96 (2H, d, *J* = 8.8 Hz), 6.92 (2H, d, *J* = 8.7 Hz), 3.87 (3H, s, OCH$_3$), 3.83 (3H, s, OCH$_3$). ^{13}C NMR (CDCl$_3$): 188.6, 163.2, 161.4, 143.7, 131.2, 130.6, 130.0, 127.7, 119.4, 114.3, 113.7, 55.4, 55.3. EI-MS *m/z* (%): 268 (M$^+$, 100) [23].

(E)-1-(4-Methoxyphenyl)-3-(4-(dimethylamino)phenyl)prop-2-en-1-one (164). Yield: 99%. Mp 122–124 °C. IR: 3079, 2979, 2933, 1648, 1579, 1546, 1522, 1435, 1252, 1231, 1162 cm^{-1}. ^{1}H NMR (CDCl$_3$): 8.03 (2H, d, *J* = 8.9 Hz), 7.78 (1H, d, *J* = 15.4 Hz, Hβ), 7.55

(2H, d, J = 8.6 Hz), 7.36 (1H, d, J = 15.4 Hz, Hα), 6.97 (2H, d, J = 8.9 Hz), 6.69 (2H, d, J = 8.6 Hz), 3.88 (3H, s, OCH$_3$), 4.04 (6H, s, N(CH$_3$)$_2$). ^{13}C NMR (CDCl$_3$): 188.9, 162.9, 151.9, 144.9, 131.8, 130.5, 130.2, 122.8, 116.4, 113.6, 111.8, 55.4, 40.1. EI-MS *m/z* (%): 281 (M$^+$, 100) [23].

(*E*)-3-(4-Hydroxy-3-methoxyphenyl)-1-(4-methoxyphenyl)prop-2-en-1-one (165). Yield: 63%. Mp 160–164 °C. IR: 3025, 2974, 2922, 1649, 1599, 1583, 1513, 1466, 1425, 1258, 1245, 1169 cm^{-1}. ^{1}H NMR (CDCl$_3$): 8.03 (2H, d, J = 8.7 Hz), 7.74 (1H, d, J = 15.6 Hz, Hβ), 7.39 (1H, d, J = 15.6 Hz, Hα), 7.22 (1H, d, J = 8.2 Hz), 7.13 (1H, s), 6.98 (2H, d, J = 8.7 Hz), 6.95 (1H, d, J = 8.2 Hz), 5.95 (1H, bs, OH), 3.96 (3H, s, OCH$_3$), 3.89 (3H, s, OCH$_3$). ^{13}C NMR (CDCl$_3$): 188.8, 163.3, 148.1, 146.8, 144.3, 131.3, 130.7, 127.7, 123.1, 119.6, 114.8, 113.8, 110.0, 56.0, 55.5. EI-MS *m/z* (%): 284 (M$^+$, 100) [23].

(*E*)-1,3-Diphenylprop-2-en-1-one (166). Yield: 99%. Mp 65–69 °C. IR: 3134, 1669, 1592, 1548, 1514 cm^{-1}. ^{1}H NMR (CDCl$_3$): 8.03 (2H, d, J = 7.5 Hz), 7.82 (1H, d, J = 15.6 Hz, Hβ), 7.66–7.64 (2H, m), 7.59 (1H, t, J = 7.5, Hz), 7.54 (1H, d, J = 15.6 Hz, Hα), 7.52 (2H, d, J = 7.5 Hz), 7.43–7.40 (3H, m). ^{13}C NMR (CDCl$_3$): 190.5, 144.8, 138.2, 134.8, 132.7, 130.5, 128.9, 128.6, 128.5, 128.4, 122.1. EI-MS *m/z* (%): 208 (M$^+$, 100) [24].

(*E*)-3-(2-Hydroxyphenyl)-1-phenylprop-2-en-1-one (167). Yield: 46%. Mp 154–155 °C. IR: 3421, 3025, 1650, 1600, 1556, 1505, 1176 cm^{-1}. ^{1}H NMR (CDCl$_3$): 8.14 (1H, d, J = 15.8 Hz, Hβ), 8.04 (2H, d, J = 7.5 Hz), 7.70 (1H, d, J = 15.8 Hz, Hα), 7.59 (1H, t, J = 7.5 Hz), 7.59 (1H, d, J = 7.6 Hz), 7.53–7.51 (2H, m), 7.28 (1H, d, J = 6.9 Hz), 6.97 (1H, d, J = 7.5 Hz), 6.91 (1H, d, J = 8.2 Hz). ^{13}C NMR (CDCl$_3$): 191.8, 156.0, 141.0, 138.3, 132.7, 131.8, 129.5, 128.8, 128.6, 122.7, 122.2, 120.8, 116.7. EI-MS *m/z* (%): 224 (M$^+$, 100) [24].

(*E*)-1-Phenyl-3-(*p*-tolyl)prop-2-en-1-one (168). Yield: 43%. Mp 87–91 °C. IR: 3000, 2936, 2899, 1662, 1592, 1542, 1512, 1455 cm^{-1}. ^{1}H NMR (CDCl$_3$): 8.02 (2H, d, J = 7.6 Hz), 7.80 (1H, d, J = 15.8 Hz, Hβ), 7.60–7.56 (5H, m), 7.50 (1H, d, J = 15.8 Hz, Hα), 7.23 (2H, d, J = 7.6 Hz), 2.40 (3H, s, CH$_3$). ^{13}C NMR (CDCl$_3$): 190.6, 144.9, 141.0, 138.3, 132.6, 132.1, 129.7, 128.5, 128.4, 128.4, 121.1, 21.5. EI-MS *m/z* (%): 222 (M$^+$, 100) [24].

(*E*)-3-(4-Hydroxyphenyl)-1-phenylprop-2-en-1-one (169). Yield: 85%. Mp 183–187 °C. IR: 3421, 3024, 1647, 1594, 1566, 1513, 1180 cm^{-1}. ^{1}H NMR (Acetone-*d$_6$*): 8.11 (2H, d, J = 8.4 Hz), 7.75 (1H, d, J = 15.6 Hz, Hβ), 7.71 (2H, d, J = 8.9 Hz), 7.61 (1H, t, J = 8.4 Hz), 7.54 (2H, d, J = 8.4 Hz), 7.53 (1H, d, J = 15.6 Hz, Hα), 6.92 (2H, d, J = 8.9 Hz). ^{13}C NMR (Acetone-*d$_6$*): 189.9, 160.8, 145.2, 139.4, 133.3, 131.5, 129.4, 129.1, 127.5, 119.6, 116.7. EI-MS *m/z* (%): 224 (M$^+$, 100) [24].

(*E*)-3-(4-Methoxyphenyl)-1-phenylprop-2-en-1-one (170). Yield: 99%. Mp 70–72 °C. IR: 3066, 2929, 1662, 1596, 1546, 1511, 1466, 1239, 1214 cm^{-1}. ^{1}H NMR (CDCl$_3$): 8.01 (2H, d, J = 7.5 Hz), 7.89 (1H, d, J = 15.6 Hz, Hβ), 7.60 (2H, d, J = 8.7 Hz), 7.57 (1H, t, J = 7.5 Hz), 7.49 (2H, d, J = 7.5 Hz), 7.42 (1H, d, J = 15.6 Hz, Hα), 6.93 (2H, d, J = 8.7 Hz), 3.85 (3H, s, OCH$_3$). ^{13}C NMR (CDCl$_3$): 190.5, 161.6, 144.7, 138.4, 132.5, 130.2, 128.5, 128.4, 127.5, 119.7, 114.4, 55.4. EI-MS *m/z* (%): 238 (M$^+$, 100) [24].

(*E*)-3-(2-Hydroxy-3-methoxyphenyl)-1-phenylprop-2-en-1-one (171). Yield: 68%. Mp 107–109 °C. IR: 3383, 2914, 1665, 1598, 1479, 1249, 1222 cm^{-1}. ^{1}H NMR (CDCl$_3$): 8.04 (1H, d, J = 15.7 Hz, Hβ), 8.03 (2H, d, J = 7.5 Hz), 7.51 (1H, d, J = 15.7, Hα), 7.56 (1H, t, J = 6.9 Hz), 7.48 (2H, d, J = 7.5 Hz), 7.18 (1H, t, J = 7.5 Hz), 6.88–6.84 (2H, m), 6.44 (1H, bs, OH), 3.88 (3H, s, OCH$_3$). ^{13}C NMR (CDCl$_3$): 191.1, 146.8, 145.8, 140.1, 138.3, 132.4, 128.4, 123.2, 121.5, 121.3, 119.6, 111.9, 56.1. EI-MS *m/z* (%): 254 (M$^+$, 100) [24].

(*E*)-3-(2-Hydroxy-3-nitrophenyl)-1-phenylprop-2-en-1-one (172). Yield: 66%. Mp 134–138 °C. IR: 3211, 1687, 1607, 1534, 1322, 1234 cm^{-1}. ^{1}H NMR (Acetone-*d$_6$*): 8.33 (1H, d, J = 7.9 Hz), 8.22 (1H, d, J = 7.9 Hz), 8.15 (2H, d, J = 7.2 Hz), 8.14 (1H, d, J = 15.9 Hz, Hβ), 8.00 (1H, d, J = 15.9 Hz, Hα), 7.65 (1H, t, J = 7.2 Hz), 7.56 (2H, d, J = 7.2 Hz), 7.18 (1H, t, J = 7.9 Hz). ^{13}C NMR (Acetone-*d$_6$*): 189.8, 154.2, 138.8, 136.9, 135.5, 133.8, 12.6, 129.3, 127.6, 127.1, 125.2, 120.8. EI-

MS *m/z* (%): 269 (M$^+$, 100) [24].

(*E*)-3-(4-Hydroxy-3-nitrophenyl)-1-phenylprop-2-en-1-one (173). Yield: 75%. Mp 81–83 °C. IR: 3217, 3072, 1659, 1605, 1536, 1493, 1353 cm^{-1}. ^{1}H NMR (CDCl$_3$): 10.76 (1H, s, OH), 8.39 (1H, d, J = 1.4 Hz), 8.03 (2H, d, J = 7.3 Hz), 7.88 (1H, dd, J = 8.7, 1.4 Hz), 7.74 (1H, d, J = 15.7 Hz, Hβ), 7.64–7.53 (3H, m), 7.51 (1H, d, J = 15.7 Hz, Hα), 7.24 (1H, d, J = 8.7 Hz). ^{13}C NMR (CDCl$_3$): 189.8, 156.3, 141.5, 137.8, 136.5, 133.8, 133.1, 128.8, 128.5, 127.8, 125.0, 122.6, 120.9. EI-MS *m/z* (%): 269 (M$^+$, 100) [35].

6.3. Determination of in vitro MAO activity

The effects of the chalcone derivatives on *h*MAO enzymatic activity were evaluated by a fluorometric method following the experimental protocol previously described by us. Briefly, 50 μL of sodium phosphate buffer (0.05 M, pH 7.4) containing the test molecules (compounds or reference inhibitors) in different concentrations and adequate amounts of recombinant *h*MAO-A or *h*MAO-B [adjusted to obtain in our experimental conditions the same reaction velocity (*h*MAO-A: 1.1 μg protein; specific activity: 150 nmol of *p*-tyramine oxidized to *p*-hydroxyphenylacetaldehyde/min/mg protein; *h*MAO-B: 7.5 μg protein; specific activity: 22 nmol of *p*-tyramine transformed/ min/mg protein)] were incubated for 10 min at 37 °C in a flat-black bottom 96-well microtest plate, placed in the dark fluorimeter chamber. After this incubation period, the reaction was started by adding 50 μL of the mixture containing (final concentrations) 200 μM of the Amplex® Red reagent, 1 U/mL of horseradish peroxidase and 1 mM of *p*-tyramine. The production of H$_2$O$_2$ and, consequently, of resorufin, was quantified at 37 °C in a multidetection microplate fluorescence reader (Fluo-star OptimaTM, BMG LABTECH, Offenburg, Germany) based on the fluorescence generated (excitation, 545 nm, emission, 590 nm) over a 10 min period, in which the fluorescence increased linearly. Control experiments were carried out simultaneously by replacing the tested molecules with appropriate dilutions of the vehicles. In addition, the possible capacity of these molecules to modify the fluorescence generated in the reaction mixture, due to non-enzymatic inhibition (i.e. for directly reacting with Amplex® Red reagent), was determined by adding these molecules to solutions containing only the Amplex® Red reagent in sodium phosphate buffer. The specific fluorescence emission (used to obtain the final results) was calculated after subtraction of the background activity, which was determined from wells containing all components except the *h*MAO isoforms, which were replaced by sodium phosphate buffer solution.

Declaration of Competing Interest

The authors declare that they have no known competing financial interests or personal relationships that could have appeared to influence the work reported in this paper.

Acknowledgements

Appendix A. Supplementary material

Supplementary data to this article can be found online at https://doi.org/10.1016/j.bioorg.2021.104689.

References

[1] C.L. Zhuang, W. Zhang, C.Q. Sheng, W.N. Zhang, C.G. Xing, Z.Y. Miao, Chalcone: A privileged structure in medicinal chemistry, Chem. Rev. 117 (12) (2017) 7762–7810.

[2] M.N. Gomes, E.N. Muratov, M. Pereira, J.C. Peixoto, L.P. Rosseto, P.V.L. Cravo, C. H. Andrade, B.J. Neves, Chalcone derivatives: Promising starting points for drug design, Molecules 22 (8) (2017) 1210.

[3] M.J. Matos, S. Vazquez-Rodriguez, E. Uriarte, L. Santana, Potential pharmacological uses of chalcones: a patent review (from June 2011–2014), Exp. Opin. Ther. Pat. 25 (3) (2015) 351–366.

[4] G. Lopez, M. Mellado, E. Werner, B. Said, P. Godoy, N. Caro, X. Besoain, I. Montenegro, A. Madrid, Sonochemical synthesis of 2'-hydroxychalcone derivatives with potential anti-oomycete activity, Antibiotics 9 (9) (2020) 576.

[5] I. Montenegro, O. Munoz, J. Villena, E. Werner, M. Mellado, I. Ramirez, N. Caro, S. Flores, A. Madrid, Structure-activity relationship of dialkoxychalcones to combat fish pathogen *Saprolegnia australis*, Molecules 23 (6) (2018) 1377.

[6] S. Verma, A.K. Srivastava, O.P. Pandey, A review on chalcones synthesis and their biological activity, PharmaTutor 6 (2) (2018) 22–39.

[7] S. Vazquez-Rodriguez, S. Vilar, S. Kachler, K.N. Klotz, E. Uriarte, F. Borges, M. J. Matos, Adenosine receptor ligands: Coumarin-chalcone hybrids as modulating agents on the activity of hARs, Molecules 25 (18) (2020) 4306.

[8] S. Vazquez-Rodriguez, R. Figueroa-Guinez, M.J. Matos, C. Olea-Azar, J.D. Maya, E. Uriarte, L. Santana, Facing Chagas' disease: Trypanocidal properties of new coumarin-chalcone scaffolds, Med. Chem. 12 (6) (2016) 537–543.

[9] F. Perez-Cruz, S. Vazquez-Rodriguez, M.J. Matos, A. Herrera-Morales, F. A. Villamena, A. Das, B. Gopalakrishnan, C. Olea-Azar, L. Santana, E. Uriarte, Synthesis and electrochemical and biological studies of novel coumarin-chalcone hybrid compounds, J. Med. Chem. 56 (15) (2013) 6136–6145.

[10] S. Vazquez-Rodriguez, R. Figueroa-Guinez, M.J. Matos, L. Santana, E. Uriarte, M. Lapier, J.D. Maya, C. Olea-Azar, Synthesis of coumarin-chalcone hybrids and evaluation of their antioxidant and trypanocidal properties, MedChemComm 4 (6) (2013) 993–1000.

[11] S. Vazquez-Rodriguez, M.J. Matos, L. Santana, E. Uriarte, F. Borges, S. Kachler, K. N. Klotz, Chalcone-based derivatives as new scaffolds for hA₃ adenosine receptor antagonists, J. Pharm. Pharmacol. 65 (5) (2013) 697–703.

[12] K.F. Tipton, 90 years of monoamine oxidase: some progress and some confusion, J. Neural. Transm. 125 (11) (2018) 1519–1551.

[13] R.K.P. Tripathi, S.R. Ayyannan, Monoamine oxidase B inhibitors as potential neurotherapeutic agents: An overview and update, Med. Res. Rev. 39 (5) (2019) 1603–1706.

[14] B. Mathew, Unraveling the structural requirements of chalcone chemistry towards monoamine oxidase inhibition, Cent. Nerv. Syst. Agents Med. Chem. 19 (1) (2019) 6–7.

[15] B. Mathew, A. Haridas, J. Suresh, G.E. Mathew, G. Ucar, V. Jayaprakash, Monoamine oxidase inhibitory action of chalcones: A mini review, Cent. Nerv. Syst. Agents Med. Chem. 16 (2) (2016) 120–136.

[16] P. Guglielmi, B. Mathew, D. Secci, S. Carradori, Chalcones: Unearthing their therapeutic possibility as monoamine oxidase B inhibitors, Eur. J. Med. Chem. 205 (2020) 112650.

[17] M. Mellado, C.O. Salas, E. Uriarte, D. Vina, C. Jara-Gutierrez, M.J. Matos, M. Cuellar, Design, synthesis and docking calculations of prenylated chalcones as selective monoamine oxidase B inhibitors with antioxidant activity, ChemistrySelect 4 (26) (2019) 7698–7703.

[18] K. Roy, P. Chakraborty, I. Mitra, P.K. Ojha, S. Kar, R.N. Das, Some case studies on application of "r_m^2" metrics for judging quality of quantitative structure-activity

[19] relationship predictions: Emphasis on scaling of response data, J. Comput. Chem. 34 (12) (2013) 1071–1082.

[19] A. Tropsha, Best practices for QSAR model development, validation, and exploitation, Mol. Inf. 29 (6–7) (2010) 476–488.

[20] D.T. Parambi, J.M. Oh, S.C. Baek, J.P. Lee, A.R. Tondo, O. Nicolotti, H. Kim, B. Mathew, Design, synthesis and biological evaluation of oxygenated chalcones as potent and selective MAO-B inhibitors, Bioorg. Chem. 93 (2019) 103335.

[21] E. Abad, R.K. Zenn, J. Kastner, Reaction mechanism of monoamine oxidase from QM/MM calculations, J. Phys. Chem. B 117 (46) (2013) 14238–14246.

[22] M. Mellado, L. Espinoza, A. Madrid, J. Mella, E. Chavez-Weisser, K. Diaz, M. Cuellar, Design, synthesis, antifungal activity, and structure-activity relationship studies of chalcones and hybrid dihydrochromane-chalcones, Mol. Divers. 24 (3) (2020) 603–615.

[23] M. Mellado, A. Madrid, U. Martinez, J. Mella, C.O. Salas, M. Cuellar, Hansch's analysis application to chalcone synthesis by Claisen-Schmidt reaction based in DFT methodology, Chem. Pap. 72 (3) (2018) 703–709.

[24] M. Mellado, A. Madrid, M. Reyna, C. Weinstein-Oppenheimer, J. Mella, C.O. Salas, E. Sanchez, M. Cuellar, Synthesis of chalcones with antiproliferative activity on the SH-SY5Y neuroblastoma cell line: Quantitative structure-activity relationship models, Med. Chem. Res. 27 (11–12) (2018) 2414–2425.

[25] M.J. Matos, C. Teran, Y. Perez-Castillo, E. Uriarte, L. Santana, D. Vina, Synthesis and study of a series of 3-arylcoumarins as potent and selective monoamine oxidase B inhibitors, J. Med. Chem. 54 (20) (2011) 7127–7137.

[26] M. Mellado, J. Mella, C. González, D. Viña, E. Uriarte, M.J. Matos, 3-Arylcoumarins as highly potent and selective monoamine oxidase B inhibitors: Which chemical features matter? Bioorg. Chem. 101 (2020) 103964.

[27] G. Apablaza, L. Montoya, C. Morales-Verdejo, M. Mellado, M. Cuellar, C.F. Lagos, J. Soto-Delgado, H. Chung, C.D. Pessoa-Mahana, J. Mella, 2D-QSAR and 3D-QSAR/ CoMSIA studies on a series of (R)-2-((2-(1H-indol-2-yl)ethyl)amino)-1-phenylethan-1-ol with human beta(3)-adrenergic activity, Molecules 22 (3) (2017) 404.

[28] S.Y. Son, A. Ma, Y. Kondou, M. Yoshimura, E. Yamashita, T. Tsukihara, Structure of human monoamine oxidase A at 2.2-angstrom resolution: The control of opening the entry for substrates/inhibitors, Proc. Natl. Acad. Sci. U.S.A. 105 (15) (2008) 5739–5744.

[29] C. Binda, P. Newton-Vinson, F. Hubalek, D.E. Edmondson, A. Mattevi, Structure of human monoamine oxidase B, a drug target for the treatment of neurological disorders, Nat. Struct. Biol. 9 (1) (2002) 22–26.

[30] O. Trott, A.J. Olson, Software news and update AutoDock Vina: Improving the speed and accuracy of docking with a new scoring function, efficient optimization, and multithreading, J. Comput. Chem. 31 (2) (2010) 455–461.

[31] L. Schrödinger, The PyMOL Molecular Graphics System, Schrödinger, LLC, 2003–2017.

[32] R.A. Laskowski, M.B. Swindells, LigPlot+: Multiple ligand-protein interaction diagrams for drug discovery, J. Chem Inf. Model. 51 (10) (2011) 2778–2786.

[33] A.C. Wallace, R.A. Laskowski, J.M. Thornton, LigPlot - A program to generate schematic diagrams of protein ligand interactions, Protein Eng. 8 (2) (1995) 127–134.

[34] T. Narender, K.P. Reddy, A simple and highly efficient method for the synthesis of chalcones by using borontrifluoride-etherate, Tetrahedron Lett. 48 (18) (2007) 3177–3180.

[35] D.N. Rana, M.T. Chhabria, N.K. Shah, P.S. Brahmkshatriya, Discovery of new antitubercular agents by combining pyrazoline and benzoxazole pharmacophores: design, synthesis and insights into the binding interactions, Med. Chem. Res. 23 (5) (2014) 2218–2228.